Journal of Building Engineering 107 (2025) 112706

Contents lists available at ScienceDirect

Journal of Building Engineering

journal homepage: www.elsevier.com/locate/jobe

Mechanical and microstructure evolution of 3D printed concrete interlayer at elevated temperatures

Biao Zhou [a], Hongru Zhou [a], Hideki Yoshioka [b], Takafumi Noguchi [b], Kai Wang [a], Bochao Sun [c,*], Gaochuang Cai [d], Yike Guo [a], Dianchao Wang [b], Weijian Zhao [c]

[a] School of Emergency Management and Safety Engineering, China University of Mining and Technology (Beijing), Beijing, 100083, China
[b] Department of Architecture, Faculty of Engineering, The University of Tokyo, Tokyo, 113-8654, Japan
[c] College of Civil Engineering and Architecture, Zhejiang University, Hangzhou, 310058, China
[d] International Advanced Science and Technology Research Organization (IROAST), Kumamoto Univ., Kumamoto 860-8555, Japan

ARTICLE INFO

Keywords:
3D printed concrete
Interlayer crack
High temperature
Microstructure

ABSTRACT

As the technology of 3D printed concrete (3DPC) continues to advance in modern construction, understanding its fire resistance becomes increasingly important. Despite this, the performance of 3DPC under elevated temperatures—particularly in the interlayer regions, which are the weakest parts of the structure—has not been thoroughly examined. This study explores the mechanical and microstructural changes occurring in the interlayers of 3DPC when subjected to high temperatures. Through interlayer bond strength tests and advanced techniques, including X-ray Computed Tomography (CT), Scanning Electron Microscopy (SEM), X-ray Diffraction (XRD), and Thermogravimetric Analysis (TGA), it is found that elevated temperatures markedly decrease interlayer strength, leading to significant pore formation and phase transitions. Specifically, interlayer bond strength diminished by 83.1 % at 600 °C and exceeded 90 % at 800 °C. A notable increase in pore count—up by 35 % at 400 °C compared to room temperature—was also recorded. Additionally, mass loss increased significantly, reaching 13.6 % at 800 °C. These results indicate substantial degradation of structural integrity, providing critical insights for the development of more fire-resistant 3DPC materials and enhancing fire safety in construction.

1. Introduction

In recent years, 3D printing technology has rapidly developed in the construction industry, revolutionizing traditional building methods through its ability to fabricate complex geometries with reduced material waste and labor costs [1]. The technology has been successfully implemented in diverse applications ranging from residential housing prototypes [2] and pedestrian bridges [3] to emergency shelters in disaster zones. Among its applications, 3D printed concrete (3DPC) has demonstrated considerable potential due to its capacity to enhance construction efficiency, minimize material waste, and provide design flexibility. Recent advancements in material formulations have further enabled the integration of sustainable components like recycled aggregates [4] and geopolymer binders [5], positioning 3DPC as a key technology for sustainable construction. However, despite these advantages, the performance of 3DPC under extreme environmental conditions, such as high temperatures, remains inadequately explored [6]. For example, the behavior of different fibers at high temperatures is added [7], the influence of different gelling materials on the layers [8], the thermal

* Corresponding author.
E-mail addresses: zhoubiao1088@bme.arch.t.u-tokyo.ac.jp, zhoubiao1088@cumtb.edu.cn (B. Zhou), sunbochao@zju.edu.cn (B. Sun).

https://doi.org/10.1016/j.jobe.2025.112706
Received 12 February 2025; Received in revised form 6 April 2025; Accepted 16 April 2025
Available online 17 April 2025
2352-7102/© 2025 Elsevier Ltd. All rights are reserved, including those for text and data mining, AI training, and similar technologies.

performance of the building after construction [9]. In practical scenarios, particularly in the event of a fire, understanding the fire resistance of 3DPC is crucial for ensuring structural safety [10]. Therefore, studying its behavior in high-temperature environments is of paramount importance to the safety and reliability of 3DPC in construction applications.

While substantial research has been conducted on conventional concrete's performance at elevated temperatures—such as the effects on compressive strength [11], thermal expansion [12], fire spalling behavior of high-strength concrete [13]and the residual mechanical properties of concrete [14], 3DPC presents unique challenges due to its distinctive layered structure. The inherent anisotropy and interlayer porosity (The connection of the two strips caused by 3D printing is the interlayer part) created during the printing process significantly influence its thermal behavior [15,16]. For example, the evaporation of water and decomposition of hydration products such as calcium silicate hydrate (C-S-H) and calcium hydroxide ($Ca(OH)_2$) lead to microcrack formation and increased porosity, weakening the material's mechanical properties [17]. However, most current studies on 3DPC have primarily focused on its fundamental mechanical properties under standard conditions, leaving its behavior under high-temperature environments relatively underexplored.

Current research on 3D printed concrete largely focuses on its fundamental mechanical properties under standard conditions, while relatively little attention has been given to its behavior at high temperatures. The interlayer region of 3DPC is widely acknowledged as the most vulnerable zone due to two intrinsic defects, entrapped air voids formed during the staggered deposition process, and weak chemical bonding between successive layers caused by partial hydration of cement particles [18]. Micro-CT studies reveal that interlayer porosity can reach 12–18 % [19], compared to 5–8 % in cast concrete, creating stress concentration sites under thermal loading [20]. During the layer-by-layer deposition process, the bond between adjacent layers are generally weaker than the material within individual layers, resulting in increased porosity at these interfaces [21]. This elevated porosity makes the interlayer regions more susceptible to crack initiation and propagation [22]. Additionally, the anisotropic nature of 3DPC leads to significant differences in mechanical properties depending on the loading direction, with the out-of-plane strength being particularly weak [23]. When exposed to high temperatures, these weaknesses are further amplified. Current research on the interlayer region's mechanical properties and microstructure evolution at elevated temperatures remains limited, indicating the need for further investigation to clarify the mechanisms of thermal degradation.

The primary objective of this research is to investigate the effects of high-temperature exposure on the mechanical performance and microstructural evolution of 3DPC interlayer regions. Specifically, the study aims to understand how high temperatures affect the interlayer bond strength, porosity, and hydration products such as calcium silicate hydrate (C-S-H) and calcium hydroxide ($Ca(OH)_2$). To achieve this, a combination of mechanical testing and microscopic analysis methods will be employed. The research will involve interlayer bond strength tests at different temperature intervals (ranging from 200 °C to 800 °C), to evaluate the interlayer's load-bearing capacity under thermal stress. Additionally, microstructural analysis will be performed using scanning electron microscopy (SEM), X-ray diffraction (XRD), and computed tomography (CT). SEM will provide high-resolution images of the interlayer's cracks and pore structures, while XRD will be used to identify phase changes in the hydration products as the temperature rises. CT scanning will offer 3D visualizations of internal structural changes, allowing for a detailed examination of the pore network and crack propagation. By analyzing the material at different temperatures, this study aims to correlate microstructural degradation with mechanical performance, providing a comprehensive understanding of how 3DPC interlayers respond to high temperatures.

This study addresses a gap in the existing body of literature by providing a systematic analysis of the degradation mechanisms of 3DPC interlayers under high temperatures. In contrast to previous studies, which have primarily concentrated on the overall mechanical properties of 3DPC, this research provides a comprehensive analysis of the interlayer regions, which are of critical importance to the structural integrity of the material. By integrating mechanical testing with sophisticated microstructural analysis, this study presents a more comprehensive understanding of 3DPC's performance in fire scenarios. The findings of this study will contribute to the advancement of knowledge regarding the enhancement of 3DPC fire resistance, with potential applications in the improvement of building safety and the development of more resilient construction materials.

2. Materials and experimental program

2.1. Raw materials

The 3DPC utilized in this study comprises a blend of Portland cement, river sand, water, and a variety of chemical additives. The specific composition of the printing mortar is as follows (see Table 1): river sand (1000 kg/m^3), Portland cement (1000 kg/m^3), water (350 kg/m^3), nanoclay (5.00 kg/m^3), hydroxypropyl methylcellulose (HPMC) (1.30 kg/m^3), sodium gluconate (0.70 kg/m^3), and a polycarboxylate-based superplasticizer (0.50 kg/m^3). The addition of nanoclay has been shown to enhance the mechanical properties and thermal stability of concrete, as documented in previous studies [24]. The river sand, which was sourced from natural deposits, has a fineness modulus of 2.44, with a particle size distribution ranging from 0.075 mm to 1.18 mm. The cement used was P.O. 42.5 Ordinary Portland Cement, sourced from 97 Building Materials Co., Ltd., with a 28-day compressive strength of 42.5 MPa (see Table 2).

Table 1
The mixture design of 3D printable mortar.

River sand	Cement	Water	Nanoclay	HPMC	Sodium gluconate	Polycarboxylate-based superplasticizer
1000 kg/m^3	1000 kg/m^3	350 kg/m^3	5.00 kg/m^3	1.30 kg/m^3	0.70 kg/m^3	0.50 kg/m^3

The chemical composition of the cement, as determined through X-ray fluorescence (XRF) analysis, is as follows: CaO 63.75 %, SiO_2 21.44 %, Al_2O_3 4.55 %, Fe_2O_3 3.47 %, SO_3 2.43 %, MgO 2.37 %, and Na_2O 0.48 %. This ratio is the same as in the previous study [25].

To enhance the fluidity and thixotropy of the 3DPC mix, a powder-form polycarboxylate-based superplasticizer (SP) and hydroxypropyl methylcellulose (HPMC), provided by Shanghai Chenqi Chemical Science and Technology Co., Ltd., were incorporated. The inclusion of nanoclay improved both the printability and workability of the mortar, while the other additives ensured the compatibility of the mixture, optimizing its overall performance for 3D printing applications.

2.2. Test specimen fabrication

The 3DPC specimen was fabricated using a printer nozzle with a diameter of 20 mm and the printing speed is set at 20 mm/s. The width of the printed mortar strip is 20 mm and the height was 10 mm. The printer and nozzle are shown in Fig. 1. The coordinate system is defined as follows: X-axis is the nozzle movement direction with a strip width of 20 mm, Y-axis is perpendicular to nozzle movement direction and parallel to the bottom surface of the print; Z-axis is the vertical printing direction. During the printing process, the nozzle moves back and forth in an S-shaped pattern. The interlayer was directly printed by depositing two consecutive layers of material. After printing, the specimens were divided into 12 groups and placed in a curing chamber under 20°Cand humidity (100 % RH) conditions 28 days. After reaching the target curing time, the samples were cut into different sizes to evaluate the various mechanical properties of the 3D printed samples.This printing method is the same as our previous research [25].

2.3. Testing and characterization methods

2.3.1. Elevated temperature

An electric box-type high-temperature heating furnace (SX2-2.5–10A) was used to heat the test specimens. The initial temperature was set at room temperature (20 °C). In order to achieve a balance between experimental controllability and real-world fire scenarios, a two-stage heating protocol was adopted. Below 600 °C, a constant heating rate of 15 °C/min was employed to ensure gradual thermal equilibration and to avert the effects of rapid dehydration. Above 600 °C, the ISO834 standard fire curve was applied to simulate realistic high-temperature exposure (e.g., structural fire conditions). This hybrid approach enabled precise control of early-stage reactions while capturing degradation mechanisms under extreme temperatures. The specimens were heated to target temperatures of 200 °C, 400 °C, 600 °C, and 800 °C, and then maintained at these temperatures for either 1 or 2 h. The heating curve employed in this study conforms to the ISO 834 fire standard heating curve, ensuring that the thermal exposure conditions are representative of real fire scenarios. The purpose of holding the specimens for different durations (1 or 2 h) was to simulate various fire exposure scenarios and assess how prolonged exposure impacts both the interlayer bond strength and microstructure of 3DPC. Once the target temperature had been attained and maintained for the designated period, the specimens were permitted to cool naturally to ambient temperature (20 °C). This cooling method was selected to circumvent the introduction of additional thermal stresses that might be induced by rapid cooling processes. The mass loss of the specimens before and after high-temperature exposure was recorded, and their mechanical properties were subsequently tested at room temperature.

2.3.2. Mechanical testing

The interlayer bond strength was measured using an interlayer bond strength testing machine (DR-508A), with a loading rate of 0.5 mm/min, as shown in Fig. 2. The test specimens were prepared as rectangular prisms, each consisting of two printed layers with a defined interlayer region. The dimensions of each specimen were 10 mm × 20 mm × 10 mm, with the interlayer surface aligned to ensure uniform bonding between the layers. To mitigate the impact of supplementary friction at the interlayer induced by compressive stress, the following measures were implemented:

Preparation of the Specimens, the surfaces of the test specimens were meticulously polished to ensure smooth and parallel contact with the testing machine platens, thereby reducing friction-induced errors. Lubrication, a thin layer of lubricant (e.g., petroleum jelly) was applied between the specimen and the loading platens to minimize frictional constraints. The alignment of the specimens with the loading axis was executed with precision to ensure uniform stress distribution and to avert eccentric loading. Loading Rate Control: A controlled and slow loading rate was employed to avert sudden stress concentrations that could exacerbate the Poisson's effect. To ensure even force distribution during the tensile test, rubber pads were placed between the 3DPC specimens and the fixture. This setup helped prevent localized stress concentrations and ensured that the force was applied uniformly along the interlayer. The samples were secured in the fixture, and the tensile load was applied perpendicularly to the interlayer region until bond failure occurred (see Fig. 3). Experimental parameters were configured using AnyTest analysis software, which also recorded and processed the test data, allowing for the precise determination of interlayer bond strength and failure characteristics.

Table 2
The chemical composition of the utilized Portland cement.

Compounds	CaO	SiO_2	Al_2O_3	Fe_2O_3	SO_3	MgO	Na_2O
Mass proportions (%)	63.75 %	21.44 %	4.55 %	3.47 %	2.43 %	2.37 %	0.48 %

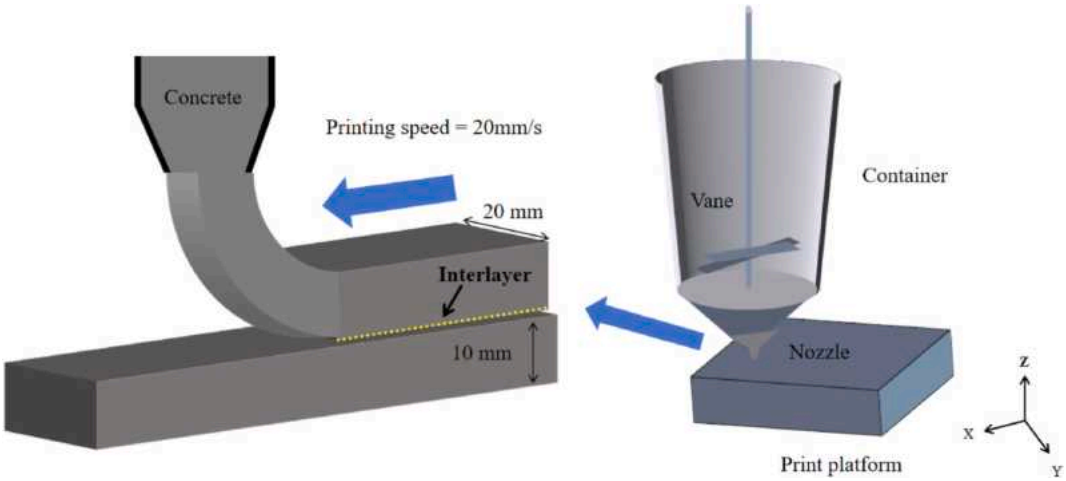

Fig. 1. 3D printing device and printing process.

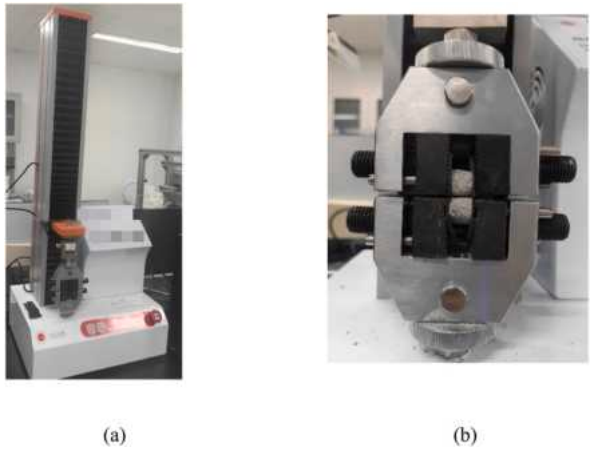

Fig. 2. Tensile test: (a) Tensile testing machine (b) 3DPC on the fixture.

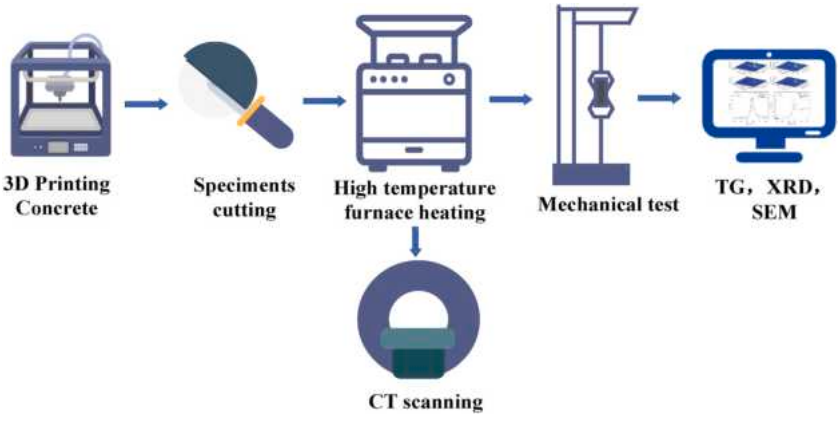

Fig. 3. Experimental process diagram.

2.3.3. CT analysis

X-ray Computed Tomography (CT) scanning was employed to provide a non-destructive 3D visualization of the internal structure of the concrete interlayer. CT (NIKON XTH 320/225) offered detailed insights into the distribution of pores, cracks, and other internal features without damaging the sample. By integrating the conclusion from SEM and CT scanning, the microstructural evolution of the 3D printed concrete interlayer was obtained. These microscopic examinations provided critical insights into the behavior of the interlayers, improving the understanding of mechanical properties and degradation mechanisms.

2.3.4. X-ray diffraction and analysis

X-ray Diffraction (XRD) was employed to characterize the composition of the 3D printed concrete at elevated temperatures. After heat treatment and natural cooling to room temperature, samples were extracted specifically from the interlayer fracture regions. These extracted portions were then crushed and ground into fine powders to ensure homogeneity for XRD analysis. The XRD tests were conducted to characterize the crystalline phases present in the interlayer and to observe phase transformations caused by the thermal exposure.

An Ultima IV advanced X-ray diffractometer was used for the X-ray diffraction analysis. The mortar samples underwent a drying process and were subsequently pulverized into powders with a particle fineness below 80 μm. All preparation processes were conducted under a nitrogen environment with a purity of 100 %. The scan angle range was set from 5 to 90°, with a speed of 0.02° per second.

2.3.5. Thermogravimetric analysis

Thermogravimetric Analysis (TGA) was used to evaluate the thermal stability and composition changes of the 3D printed concrete under high-temperature conditions. Small fragments of the 3DPC specimens were first obtained by extracting material from the interlayer regions. These fragments were then ground into fine powders to ensure uniformity for analysis. The powder samples were then directly heated from room temperature in a nitrogen atmosphere to prevent oxidation during the heating process. The heating rate was set at 10 °C/min, and the specimens were heated continuously up to 900 °C. This method involves heating the concrete samples at a controlled rate while continuously recording their weight loss. The resulting thermogram reveals critical information about the decomposition temperatures, thermal degradation behavior, and the presence of volatile compounds. By analyzing the weight loss curves, we can gain insights into the decomposition stages of the material, which helps in understanding its thermal stability and identifying any temperature-sensitive components within its microstructure.

2.3.6. SEM analysis

The pore structure will significantly affect mechanical properties and the thermal behavior of concrete. The micro-structure was observed using scanning electron microscope (SEM), SEM provides high-resolution images that reveal the distribution and size of pores, cracks, and other microstructural features. Energy Dispersive X-ray Spectroscopy (EDS) was conducted with SEM to analyze the elemental composition of the concrete. The instrument is Hitachi Regulus8100.

3. Results and discussion

3.1. Mass loss rate

The mass loss rate of 3DPC was evaluated under various temperature conditions, and the results are shown in Fig. 4. As the temperature increases, a noticeable change in the mass loss rate can be observed, particularly at higher temperatures. At 200 °C, the material exhibits a modest mass loss, primarily due to the evaporation of free and bound water within the concrete [26]. After 1 h of exposure at 200 °C, the mass loss rate reaches 4.4 %, which slightly increases to 4.8 % after 2 h, suggesting a relatively stable rate of water evaporation at this temperature. At 400 °C, the mass loss becomes more pronounced, reaching 8.95 % after 1 h and 9.2 % after 2 h. This temperature marks a critical point where bound water in calcium silicate hydrate (C-S-H) starts to decompose, leading to a more

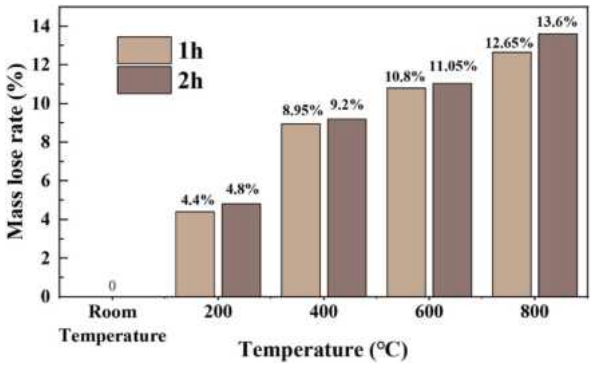

Fig. 4. Mass loss rate of 3D printed concrete at different temperatures(RT, 200 °C, 400 °C, 600 °C, 800 °C).

significant mass loss [27]. Interestingly, the difference in mass loss between 1 h and 2 h at this temperature is relatively small, suggesting that most of the decomposition occurs within the first hour, with slower progression afterward. At 600 °C, the mass loss rate continues to increase, reaching 10.8 % after 1 h and 11.05 % after 2 h. This is attributed to the breakdown of $Ca(OH)_2$ (calcium hydroxide) and other hydrated phases, which release additional water and cause a more noticeable loss of mass. The difference between 1 h and 2 h at this temperature indicates that the material continues to decompose over time, but the rate of mass loss slows as the available bound water decreases. Finally, at 800 °C, the mass loss rate reaches its highest values—12.65 % after 1 h and 13.6 % after 2 h. At this stage, the decomposition of $CaCO_3$ into CaO and CO_2 becomes significant. The release of CO_2 gas contributes to the mass loss, and the breakdown of any remaining organic additives or impurities in the concrete further accelerates the degradation process. The more substantial difference in mass loss between 1 h and 2 h at this temperature suggests that prolonged exposure to extreme temperatures leads to continued decomposition and further structural breakdown [26].

In summary, a general pattern can be observed: the mass loss rate increases with rising temperatures, and while the difference between 1 and 2 h of exposure is relatively small at lower temperatures, it becomes more pronounced at higher temperatures (600 °C and 800 °C). This indicates that prolonged exposure has a more significant effect as the temperature increases, particularly due to the decomposition of major components such as $Ca(OH)_2$ and $CaCO_3$.

3.2. Interlayer bond strength

The interlayer bond strength of 3D-printed concrete (3DPC) was measured after exposure to a range of elevated temperatures for durations of 1 and 2 h. The comparable bond strength between adjacent and stacked samples suggests that interlayer adhesion in 3D printed concrete is dominated by material-specific factors rather than geometric arrangements under the tested conditions. The comparable porosity and hydration products between adjacent and stacked layers minimized structural anisotropy. Printing process constraints, the nozzle path and layer deposition interval (20 mm/s) standardized interlayer contact quality, reducing variability across sample types. This evaluation of bond strength degradation under thermal conditions provides insight into the macroscopic effects of high temperatures on the structural integrity of 3DPC. Data presented in Fig. 5 illustrate the correlation between temperature, exposure time, and the interlayer bond strength of 3DPC, highlighting progressive strength losses as exposure temperature and duration increase.

At room temperature (RT), the interlayer bond strength of the 3DPC samples serves as a baseline, with values measured at 2.48 (±0.14) MPa for adjacent samples and 2.68 (±0.19) MPa for stack samples. These baseline measurements enable a comparative analysis of the effects of thermal exposure on 3DPC bond strength. At 200 °C, the interlayer bond strength of adjacent samples decreases to 2.36 (±0.08) MPa after 1 h, marking a 4.8 % reduction. Following 2 h of exposure, the bond strength drops further to 2.28 (±0.06) MPa, indicating a total reduction of 8.1 %. Similarly, the bond strength of stacked samples declines to 2.56 (±0.12) MPa after 1 h (4.5 % reduction) and further decreases to 2.42 (±0.07) MPa after 2 h (9.7 % reduction). These moderate reductions at 200 °C are primarily attributed to the evaporation of both free and bound water within the concrete matrix, leading to slight weakening of the material structure. When the exposure temperature rises to 400 °C, a more pronounced reduction in bond strength is observed. For adjacent samples, the interlayer bond strength drops sharply to 1.64 (±0.24) MPa after 1 h (a 33.9 % reduction) and further decreases to 0.75 (±0.32) MPa after 2 h (a substantial 69.8 % reduction). Stacked samples show a similar pattern, with bond strength reducing to 1.93 (±0.16) MPa after 1 h (27.6 % reduction) and to 0.7 (±0.19) MPa after 2 h (73.9 % reduction). The severe loss of bond strength at 400 °C can be largely attributed to the release of bound water from C-S-H phases and the development of microcracks, both of which compromise the concrete's internal structure and mechanical integrity.

As the temperature is elevated to 600 °C, further deterioration in bond strength is noted. For adjacent samples, the bond strength reduces to 1.3 (±0.08) MPa after 1 h (47.6 % reduction) and to 0.66 (±0.07) MPa after 2 h (73.4 % reduction). Stacked samples exhibit

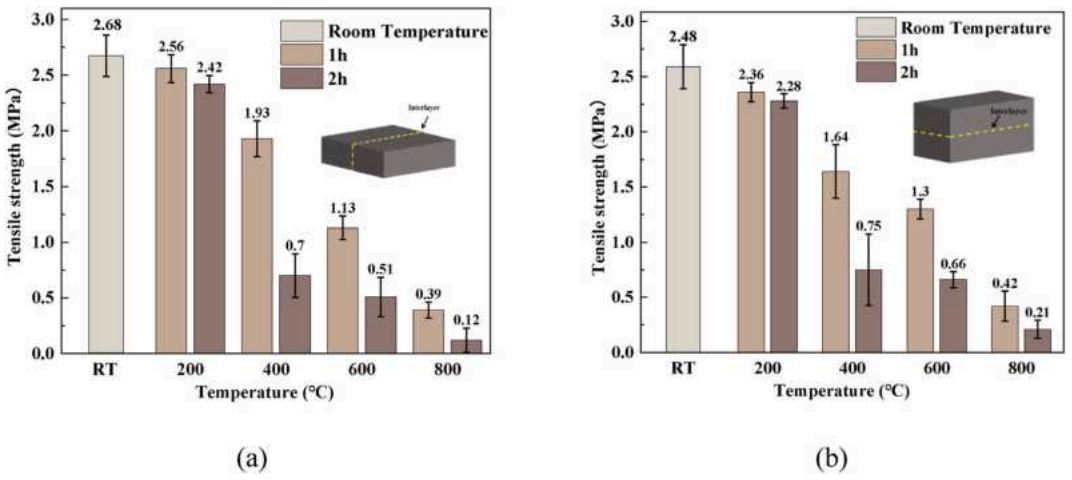

Fig. 5. Interlayer bond strength at different temperatures: (a) adjacent (b) stack.

a similar trend, with bond strength values decreasing to 1.13 (±0.1) MPa after 1 h (57.8 % reduction) and to 0.51 (±0.17) MPa after 2 h (81.0 % reduction). The reductions at this temperature are attributed to the decomposition of $Ca(OH)_2$. Exposure to 800 °C results in the most dramatic reductions in interlayer bond strength. In adjacent samples, bond strength decreases to 0.42 (±0.13) MPa after 1 h, representing an 83.1 % reduction, and further declines to 0.21 (±0.08) MPa after 2 h, totaling a 91.5 % reduction. Similarly, stacked samples experience a drop in bond strength to 0.39 (±0.07) MPa after 1 h (85.4 % reduction) and a further decrease to 0.12 (±0.1) MPa after 2 h (95.5 % reduction). At this extreme temperature, the decomposition of calcium carbonate ($CaCO_3$) and the consequent expansion of micro-cracks lead to significant loss of mechanical strength, undermining the interlayer bonds and markedly diminishing the material's structural integrity [28,29].

3.3. Microstructure and pore structure analysis

3.3.1. CT analysis

X-ray computed tomography (X-CT) is a non-destructive imaging technique that enables visualization of the internal structure of samples, allowing detailed examination of pore structures within 3D-printed concrete (3DPC) specimens subjected to various temperatures. The X-CT scans revealed the pore structures of these specimens across different temperature conditions, with experimental results displayed in Fig. 6. Using threshold segmentation and pore counting, the pore distribution across different diameter ranges was quantified, as depicted in Fig. 7.

The CT analysis revealed two distinct trends in the pore structure evolution under elevated temperatures. Firstly, there was an increase in the proportion of small pores. Secondly, there was a gradual deterioration and enlargement of single pores. The increase in small pores can be attributed to the decomposition of hydration products and the formation of new micro-cracks at elevated temperatures, which leads to the fragmentation of larger pores into smaller ones. Concurrently, the enlargement of individual pores is probably attributable to localized stress concentration and thermal expansion, which fosters the coalescence and growth of existing pores. These phenomena are not contradictory but rather reflect different aspects of the pore structure evolution under thermal exposure. The increase in small pores is indicative of the fragmentation of the pore network, while the enlargement of single pores signifies the localized deterioration of the material. Pores and voids have been demonstrated to act as stress concentrators, thereby creating localized regions of high stress that have the potential to initiate and propagate cracks. This phenomenon is particularly deleterious in 3DPC due to the layered structure, where interlayer regions are already susceptible to stress concentrations. The presence of pores is known to have a detrimental effect on the effective cross-sectional area available to bear mechanical loads. Consequently, the material's load-bearing capacity is diminished, resulting in a reduction in both tensile and compressive strength.

Through threshold segmentation methods [30,31], the pore counts at room temperature, 200 °C, and 400 °C were recorded as 47940, 55118, and 64622, respectively. These findings indicate a progressive increase in pore count with rising temperatures—an increase of 15 % at 200 °C and 35 % at 400 °C compared with room-temperature specimens. This rise in pore quantity is particularly notable in the smallest pore size range (0–0.05 mm), where the percentage of pores at 400 °C is significantly higher than at the lower temperatures. This increased concentration of small pores at elevated temperatures is likely due to the evaporation of free and bound water, which leaves voids within the material matrix. The formation of numerous small pores introduces additional microcracks, which can further expand and coalesce, contributing to larger pore development over time. The influence of temperature on pore volume also underscores how thermal exposure alters the internal structure of 3DPC. Higher temperatures facilitate the formation of smaller pores within the sample, which, combined with increases in the number of larger pores (exceeding 0.1 mm^3), demonstrates the cumulative impact of water release and crack propagation at elevated temperatures [23]. The observed changes in pore size and volume distribution across temperature conditions are further visualized in the 3D reconstructions shown in Fig. 7, illustrating how increased pore formation and growth compromise the interlayer structure.

In 3D-printed concrete, the interlayer is a critical structural zone formed during the printing process. This region is inherently prone to cracks and pore formation, making it one of the weaker areas in the 3DPC matrix. To examine the interlayer's microstructural evolution under thermal stress, samples were subjected to X-CT analysis at varying temperatures, as illustrated in Fig. 8. The image in Fig. 8(a) is taken from the interlayer region within the normal temperature sample and provides a visualization of the interlayer porosity. The CT analysis revealed the evolution of pore structure in the same specimen under different temperatures. The global CT images (Fig. 8(a)) provide an overview of the pore distribution and density across the entire specimen, while the local images (Fig. 8(b)

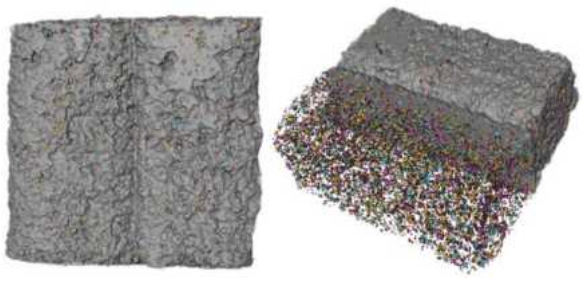

Fig. 6. X-CT scanning 3D views of interlayer pore structures in 3D printed concrete (Room Temperature).

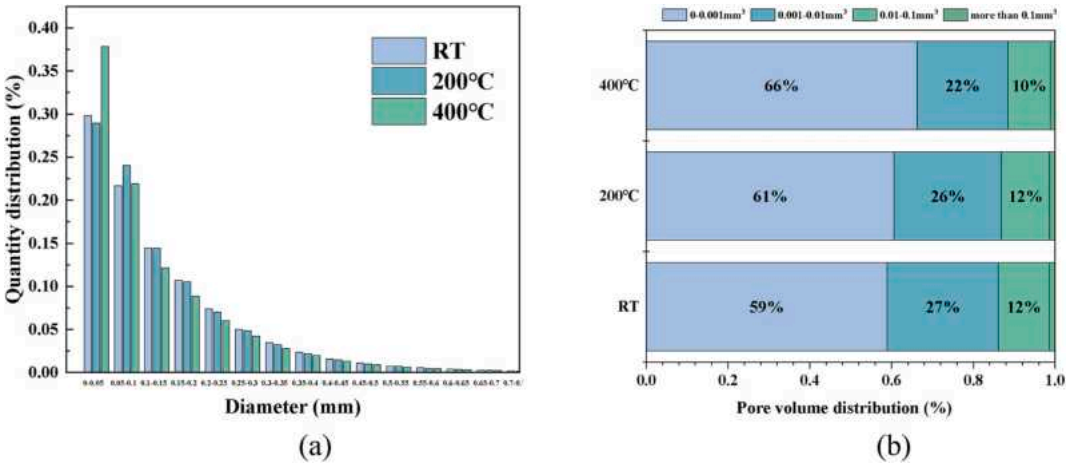

Fig. 7. Pore distribution of 3D printed concrete at different temperatures: (a) pore size distribution (b) pore volume distribution.

Fig. 8. Interlayer pore distribution of 3DPC:
(a)RT (b)Single pore structure (c)Single pore structure.

(c)) focus on specific regions to highlight the evolution of individual pores.

At 200 °C, both the number and irregularity of pores increase significantly compared to the room temperature sample shown in Fig. 8(a). This increase reflects the initial thermal-driven water loss, with partial evaporation leading to pore expansion and some merging of pores into larger voids. This structural change suggests that temperature-induced water loss within the concrete matrix initiates porosity changes that compromise the integrity of interlayer, with larger and irregular pores beginning to dominate the microstructure [23].

Upon exposure to 400 °C, a more pronounced escalation in porosity is evident. Here, the pore quantity, size, and connectivity increase substantially, with adjacent pores merging to form larger voids and cracks. This extensive porosity can be attributed to the further evaporation of bound water, coupled with the decomposition of C-S-H, a critical binder in concrete that maintains structural cohesion [32]. The formation of interconnected pores and cracks at this temperature highlights the significant weakening effect of higher thermal exposure on the interlayer, suggesting that pore expansion and structural degradation intensify with increasing temperature.

To quantify these changes, the diameter and volume of identical pores across temperature conditions were measured. In Fig. 8(b), for instance, a single pore's diameter expands from 0.52 mm at room temperature to 0.53 mm at 200 °C and 0.54 mm at 400 °C, with corresponding pore volume increases from 0.075 mm^2 to 0.079 mm^2 and 0.082 mm^2, respectively. Similarly, Fig. 8(c) presents another set of pores where diameter and volume also increase with temperature—from 0.49 mm at room temperature to 0.51 mm at 200 °C and 0.52 mm at 400 °C, while volume rises from 0.06 mm^2 to 0.07 mm^2 and finally to 0.076 mm^2. These measurements provide a quantitative view of how individual pores grow with thermal exposure, reinforcing the observation that temperature accelerates pore expansion and, ultimately, the degradation of the interlayer.

The appearance of numerous smaller pores at 400 °C, further illustrates the effects of temperature on the microstructure. These smaller pores, originating from bound water release and C-S-H decomposition, tend to merge with nearby pores, progressively forming larger cavities and cracks. This interconnected porosity intensifies the mechanical vulnerability of the interlayer, as shown by the substantial increase in pore connectivity and crack prevalence at elevated temperatures. This study of pore evolution underscores how rising temperatures adversely affect 3DPC interlayers, providing key insights into the relationship between thermal exposure, microstructural integrity, and the overall durability of 3DPC structures.

3.3.2. XRD analysis

X-ray diffraction analysis was used to characterize the phase composition of 3DPC at various temperature stages (RT, 200 °C, 400 °C, 600 °C, 800 °C), as shown in Fig. 9. The XRD patterns reveal significant changes in peak intensity and position as temperature increases, indicating phase transitions within the material [33]. At room temperature (RT), represented by the black baseline in Fig. 9, the primary components detected are silica (SiO_2) and calcium carbonate ($CaCO_3$). These compounds provide the foundational structural integrity of 3DPC. Upon heating to 200 °C (red line), most diffraction peaks remain at their original positions, indicating no major phase transformations. However, characteristic peaks of calcium hydroxide ($Ca(OH)_2$) emerge at this temperature, formed by a reaction between released water and calcium oxide (CaO). Since 200 °C is insufficient to induce significant chemical decomposition, the peaks associated with SiO_2 and $CaCO_3$ remain stable at this stage. At 400 °C (blue line), the $Ca(OH)_2$ peaks begin to diminish, suggesting the start of its thermal decomposition, while peaks of SiO_2 and $CaCO_3$ are still evident. As temperature rises, $Ca(OH)_2$ progressively decomposes due to further heating, leading to noticeable changes in its peak intensity [34]. By 600 °C (green line), $Ca(OH)_2$ decomposition is pronounced, with substantial weakening of its characteristic peaks. Additionally, slight decomposition of $CaCO_3$ begins at this temperature, as indicated by minor shifts in its peak position and a decrease in intensity. At 800 °C (purple line), the XRD pattern shows the complete disappearance of $Ca(OH)_2$ peaks, confirming its full decomposition. Concurrently, the intensity and position of SiO_2 and $CaCO_3$ peaks display slight changes, signaling minor structural alterations. $CaCO_3$ peaks are notably weakened at this temperature, reflecting its partial decomposition under extreme thermal exposure [35]. These observations illustrate the progressive transformation of 3DPC's phase composition with increasing temperature. The appearance, attenuation, and eventual disappearance of specific peaks—such as those of $Ca(OH)_2$ and $CaCO_3$—reveal critical insights into the thermal stability and degradation mechanisms within 3DPC. This analysis highlights how elevated temperatures influence the material's mineral phases, impacting the microstructural integrity and mechanical properties of 3DPC in high-temperature environments.

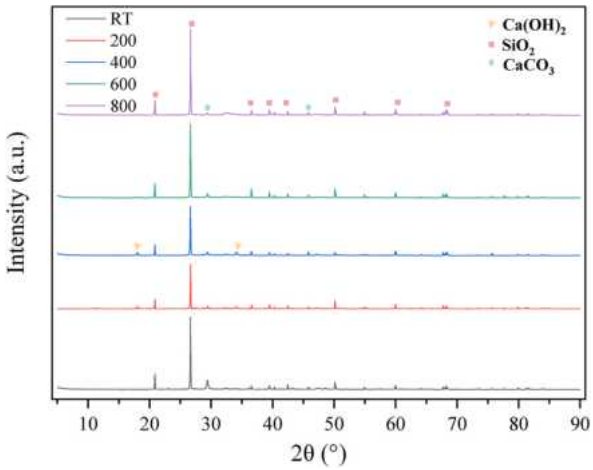

Fig. 9. XRD patterns of 3D printed concrete at different temperature stages.

3.3.3. TG analysis

The thermal decomposition behavior of 3DPC was analyzed using thermogravimetric (TG) and differential thermogravimetric (DTG). As shown in Fig. 10, a distinct weight-loss peak at a rate of 0.4485 %/min appears near 90 °C on the DTG curve. This peak corresponds primarily to the dehydration of bound water within ettringite (Aft) and C-S-H, indicating an early stage of moisture release as these phases lose absorbed and weakly bound water [35,36]. The evaporation of free and physically bound water, leading to an initial reduction in tensile strength due to weakening of the cementitious matrix. As the temperature rises to around 380 °C, a pronounced weight-loss step is observed, marking the complete volatilization of moisture-related compounds. The next major thermal event, occurring between 380 and 580 °C, is attributed to the removal of structural water, primarily associated with the degradation of $Ca(OH)_2$. This phase contributes to a significant weight reduction as $Ca(OH)_2$ decomposes into CaO and water vapor. These thermal events align with the mechanical data presented in Section 3.1, where a sharp decline in tensile strength was observed at temperatures above 400 °C. The decomposition of $Ca(OH)_2$ and other hydration products at elevated temperatures contributes to the increased porosity and reduced load-bearing capacity of the material. At temperatures above 580 °C, the continued weight loss is due to the decomposition of calcium carbonate ($CaCO_3$). This stage, designated as the 580–800 °C interval, represents the breakdown of $CaCO_3$ into calcium oxide (CaO) and carbon dioxide (CO_2), resulting in a marked decrease in material mass. The final, slower rate of weight loss beyond 800 °C is attributed to the gradual carbonization of silicate phases within the concrete. Even at 900 °C, substantial residual material remains, consisting of thermally stable components such as quartz, residual C-S-H, and calcite. To quantify the composition of chemically bound water and $Ca(OH)_2$, the thermogravimetric curve was divided into specific stages based on temperature ranges and corresponding reactions [37]. Stage A (room temperature to 380 °C) primarily involves the loss of chemically bound water from Aft and C-S-H. Stage B (380–580 °C) captures the decomposition of $Ca(OH)_2$, which peaks around 410 °C, reflecting the release of structural water. Finally, Stage C (580–800 °C) corresponds to the decomposition of $CaCO_3$, with a characteristic peak near 660 °C.

The calculation formula is as follows:

$$m(H_2O) = m_A + m_B + m_C \times \frac{18}{44}$$

$$m(Ca(OH)_2) = m_B \times \frac{74}{18} + m_C \times \frac{74}{44}$$

Where, m_A, m_B and m_C are the mass loss of each stage, 18 and 44 are the relative molecular mass of water and carbon dioxide, respectively, and the calculation results are shown in Table 3 (See. Table 2)

3.3.4. SEM analysis

The degradation of crystalline structures in the interlayer significantly impacts the mechanical performance of 3DPC under high-temperature conditions. This region, already more porous and mechanically weaker due to its layer-by-layer construction, undergoes rapid deterioration of essential hydration products—primarily C-S-H and calcium hydroxide - as temperature rises. These transformations lead to a marked reduction in the interlayer's load-bearing capability, directly correlating with the observed decline in mechanical strength during bond strength testing. The SEM images were taken specifically from the interlayer region to investigate the bonding characteristics and microstructural changes induced by elevated temperatures. The selection of the interlayer region was based on its critical role in determining the mechanical performance of 3DPC as it is the most fragile part of the layered structure.

At room temperature, the C-S-H gel exists in a dense, fibrous network of small, plate-like structures, which forms the main source of bonding strength in concrete. In 3DPC, the C-S-H gel adheres tightly to aggregate surfaces and bridges gaps between printed layers, enabling effective load transfer across interlayer boundaries. This network contributes significantly to the cohesive properties within

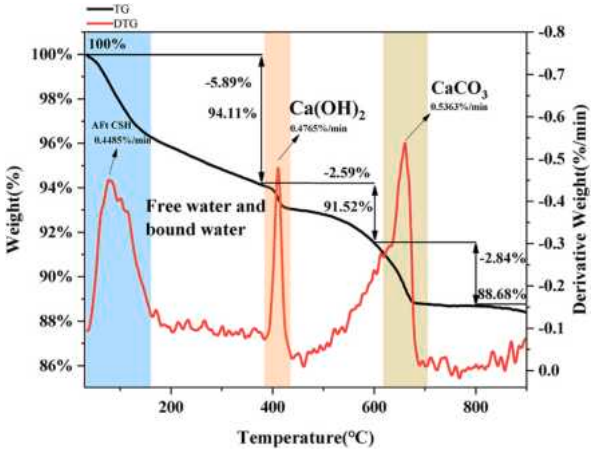

Fig. 10. Differential Thermogravimetric (DTG) and Thermogravimetric (TG) curves of 3D printed concrete: demonstrate the main weight loss stages, corresponding to the dehydration of C-S-H, $Ca(OH)_2$ breakdown, and $CaCO_3$ decarbonation under rising temperatures.

Table 3
Dehydration and decomposition percentages of key hydration phases in 3D printed concrete at elevated temperatures.

Dehydration of C-S-H(%)	Dehydration of $Ca(OH)_2$ (%)	Decomposition of $CaCO_3$(%)	m(H_2O) (%)	m($Ca(OH)_2$) (%)
5.89	2.59	2.84	9.64	15.43

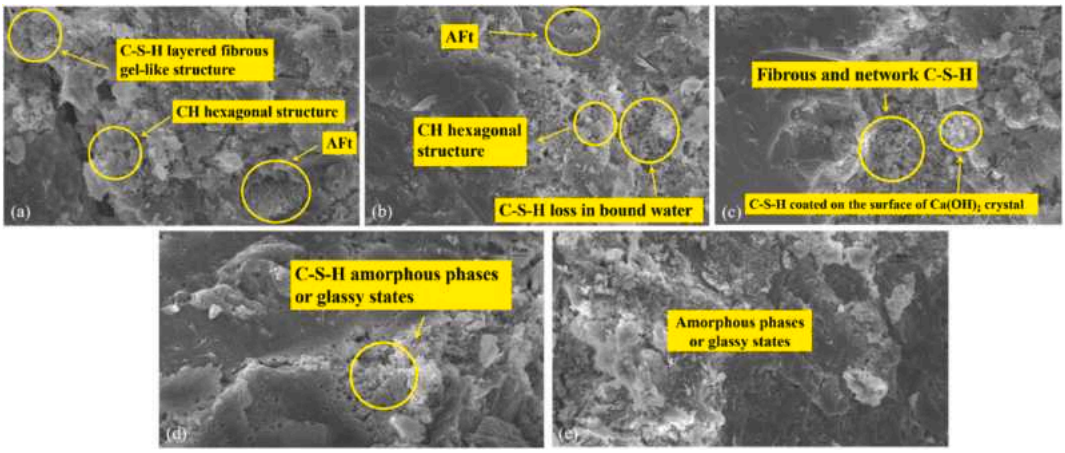

Fig. 11. SEM images of microstructure and hydration products with 3DPC interlayer at different temperature: (a) RT (b) 200 °C (c) 400 °C (d) 600 °C (e) 800 °C.

the interlayer, which is essential for the structural integrity of printed concrete.

Upon exposure to 200 °C, illustrated by the morphology in Fig. 11(b), the C-S-H gel begins to undergo dehydration, resulting in the partial breakdown of its fibrous network. SEM images reveal the thinning of the gel, as individual plate-like structures start to separate slightly, causing a reduction in cohesion. Although the overall structure remains largely intact, this early-stage dehydration initiates microcrack formation within the interlayer. At this stage, $Ca(OH)_2$ retains its hexagonal crystalline structure, although minor stress-induced degradation can be seen at the crystal edges near these microcracks. While some load-bearing capacity is maintained, the combined effects of C-S-H dehydration and microcracking reduce interlayer bond strength, as the weakened C-S-H network can no longer bind the printed layers as effectively.

At 400 °C, shown in Fig. 11(c), the C-S-H gel undergoes further dehydration, resulting in extensive fragmentation of the fibrous network. The formerly cohesive structure begins to disintegrate, as plate-like particles separate more significantly, leading to the formation of larger cracks and voids in the interlayer. The loss of water in the C-S-H gel greatly diminishes the bonding strength between layers, as the gel can no longer sustain its cohesive properties. Additionally, $Ca(OH)_2$ starts decomposing at around 400 °C, transforming into CaO and releasing water vapor. The hexagonal $Ca(OH)_2$ crystals become structurally unstable, with visible erosion and disintegration of their edges.

As $Ca(OH)_2$ decomposes, the interlayer loses a crucial reinforcing phase, further weakening its capacity for load transfer. The released water vapor contributes to additional microcracking and pore formation, compounding the degradation effects. This combined loss of C-S-H cohesion and $Ca(OH)_2$ stability accounts for the observed 70 % reduction in interlayer bond strength at 400 °C. At this point, the interlayer displays extensive cracking and a significantly reduced load-bearing capability, as the remaining hydration products are no longer capable of maintaining structural integrity within the 3DPC. This analysis highlights the critical role of temperature-induced phase transformations in determining the structural resilience of 3DPC, emphasizing the vulnerability of the interlayer at elevated temperatures [38,39].

At 600 °C, as shown in Fig. 11(d), the structural degradation of the 3DPC interlayer accelerates. The C-S-H gel, previously responsible for the fibrous and cohesive nature of the interlayer, has largely decomposed. This breakdown transforms what was once a robust, load-bearing network into a fragmented and porous structure, leaving large voids and cracks that drastically reduce the ability of interlayer to sustain mechanical loads. With the loss of C-S-H, the interlayer can no longer effectively transfer stresses across the printed layers. The $Ca(OH)_2$ has also fully decomposed into CaO by this temperature, further destabilizing the interlayer. $Ca(OH)_2$ originally acted as a stabilizing phase within the concrete, and its decomposition results in a highly porous interlayer with weakened bonding between particles. The absence of $Ca(OH)_2$ exacerbates structural instability, as large interconnected pores further compromise load-bearing capabilities. Additionally, at 600 °C, calcium carbonate ($CaCO_3$) begins to decompose, initiating its transformation into CaO and releasing carbon dioxide gas. Although $CaCO_3$ is stable up to around 700 °C, decomposition starts earlier at 600 °C under thermal stress. This process generates new pores as CO_2 escapes, increasing the void content and contributing to additional cracks within the already degraded interlayer. These transformations indicate the beginning of major structural collapse as porosity increases and cohesive material phases are lost.

By 800 °C, shown in Fig. 11(e), the interlayer reaches near-total failure. The decomposition of both C-S-H and $Ca(OH)_2$ is complete,

leaving the interlayer devoid of the essential hydration products that provided initial structural integrity. This phase of degradation introduces large, interconnected pores and extensive cracks throughout the interlayer, eliminating its ability to carry any significant mechanical loads. The accelerated decomposition of $CaCO_3$ further weakens the interlayer, producing more voids as CO_2 release continues and the material becomes increasingly brittle. At this stage, the interlayer bond strength has declined by over 90 %, leading to a near-complete structural collapse. With $CaCO_3$ decomposed and no stabilizing hydration products left, the interlayer is characterized by an interconnected network of cracks and voids that undermine the material's cohesion entirely. The matrix of CaO that remains is brittle and unable to support loads, resulting in catastrophic failure of the interlayer. This combination of $CaCO_3$ decomposition, increased porosity, and widespread cracking signals the complete structural breakdown of the 3DPC interlayer under extreme thermal conditions.

The interlayer region in 3DPC is particularly vulnerable due to the inherent discontinuities introduced by the layer-by-layer printing process. This region is characterized by higher porosity and weaker bonds between layers, making it susceptible to crack formation and propagation under thermal stress. As temperature rises, the degradation of this interlayer is directly linked to the overall reduction in mechanical strength.

At 200 °C, as illustrated in Fig. 12 (a) and **(b)**, SEM images reveal the onset of microcracks in the interlayer. These cracks, though small, signal the beginning of structural damage, where the inherent porosity of the interlayer concentrates stress, increasing susceptibility to thermal degradation. The primary mechanism for this early damage is the evaporation of free and bound water from the concrete matrix, voids are left behind, particularly in areas with higher initial moisture content, leading to microcracks that weaken local cohesion [40,41]. This reduction in contact between cementitious particles diminishes the interlayer's load-bearing capacity, corresponding to the minor decrease in bond strength observed in mechanical tests. Although structural integrity is still largely intact at this stage, these microcracks indicate the interlayer's sensitivity to thermal stress.

At 400 °C, shown in Fig. 12 (c), SEM images display a more pronounced expansion of these cracks within the interlayer. The cracks begin to interconnect, forming networks that significantly compromise the structural cohesion of the interlayer. Different thermal expansion rates of concrete components—primarily aggregates and cement paste—generate internal stresses as they expand unevenly under heat [41].These differentias lead to thermal stresses, particularly at boundaries between materials with varying thermal properties, resulting in localized fractures. This structural deterioration at 400 °C causes up to a 70 % reduction in interlayer strength, highlighting the role of thermal stress in interlayer breakdown.

When temperatures reach 600 °C, as depicted in Fig. 12 (d), the crack network within the interlayer becomes extensive, with cracks widening and deepening. At this stage, crack connectivity intensifies, creating large, continuous fissures that drastically reduce the material's load-bearing capacity. The decomposition of $Ca(OH)_2$ and $CaCO_3$ exacerbates internal stresses as water vapor and carbon dioxide are released, further propagating microcracks. These phase changes reduce the cohesive strength of the cementitious matrix, marking a critical threshold where the interlayer's structural integrity fails progressively. This extensive degradation results in a 40–80 % decrease in bond strength, emphasizing that the interlayer's weakening at this temperature plays a decisive role in the overall mechanical failure of the 3DPC structure.

At 800 °C, as illustrated in Fig. 12 (e), the extent of cracking within the concrete matrix grows substantially, with the interlayer essentially losing all structural integrity. Cracks form an interconnected network across the entire interlayer region, drastically diminishing the material's load-bearing capacity. The binding phases, particularly C-S-H gels, undergo extensive decomposition, leading to a fragmented microstructure [35]. This network of cracks and voids facilitates the easy propagation of fractures under

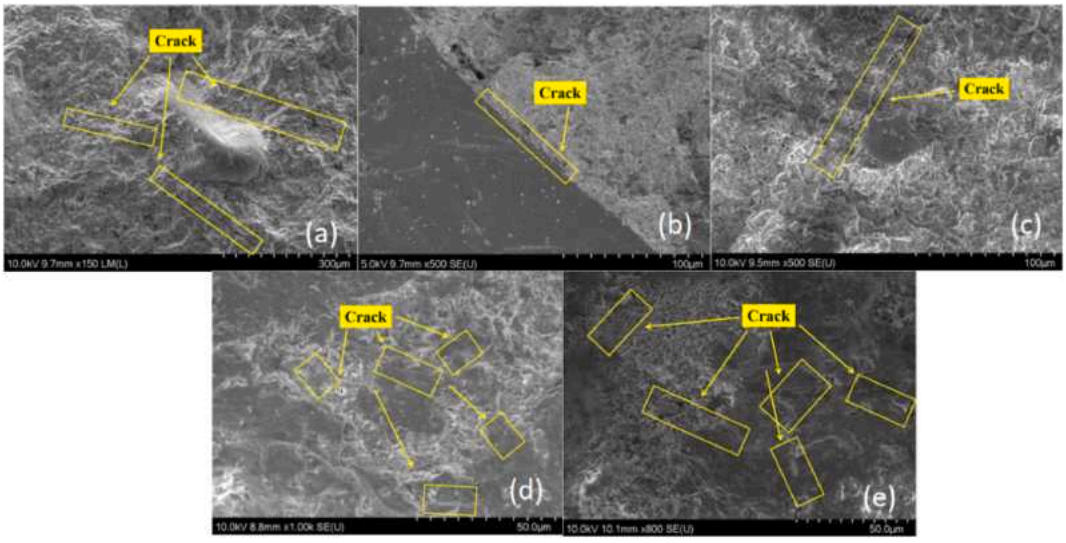

Fig. 12. SEM analysis of crack formation and morphology in 3D printed concrete at various temperatures: (a) RT (b) 200 °C (c) 400 °C (d) 600 °C (e) 800 °C.

mechanical stress, resulting in a significant reduction in material strengthges reveal that cracks are not uniformly distributed across the material. Some regions show a higher density of fractures, often coinciding with local weaknesses such as areas with greater porosity or zones where sand and cement particles are separated. These areas serve as initiation points for fractures, which then aggregate and spread throughout the matrix. The presence of these local weaknesses accelerates the degradation process, as cracks in these zones rapidly propagate, forming large, interconnected fracture networks that reduce the overall strength [42].

This development of cracks and voids further reduces the effective cross-sectional area capable of supporting mechanical loads. With the growth and interconnection of fractures, the material loses its ability to distribute and withstand external forces effectively. At elevated temperatures, particularly beyond 800 °C, the concrete's microstructure becomes exceptionally porous and fractured. This porosity and the fragmentation of the interlayer create a structure with greatly reduced carrying capacity, illustrating a nearly complete mechanical failure due to thermal degradation.

3.4. Mechanism of interlayer degradation

This study systematically examines the evolution of 3DPC properties under high-temperature conditions, focusing on both mechanical performance and microstructural changes. Results indicate that 3DPC undergoes distinct, multi-stage physical and chemical transformations when exposed to elevated temperatures, with each stage influencing the mechanical strength and microstructural integrity.

C- S-H decomposition: At temperatures below 200 °C, C-S-H is primarily stable, maintaining its layered fibrous gel-like structure, as shown in Fig. 13. The confined water significantly influences its mechanical properties, providing both flexibility and strength. As the temperature rises, water begins to evaporate, but the structural integrity of C-S-H remains relatively intact, as shown in Fig. 13. This phase provides mechanical stability due to the interlocking silicate chains, which remain connected through calcium bridging ions [43, 44]. As the temperature surpasses 200 °C, as depicted in Fig. 14(a), C-S-H undergoes progressive dehydration, leading to a marked loss in bound water. At this stage, molecular dynamics (MD) simulations reveal that water confined within and between the C-S-H layers plays a crucial role in maintaining mechanical properties [45]. As water is lost, the silicate chains in C-S-H condense, increasing hardness and stiffness initially. However, the cohesion between grains weakens due to the loss of hydration water, which can no longer lubricate the intergranular regions, leading to brittleness and crack formation. At temperatures above 400 °C, C-S-H undergoes significant structural changes, as shown in Fig. 14(b). The silicate chains that define the tobermorite-like structure of C-S-H begin to break down, transforming into more amorphous phases or glassy states [46], which dramatically reduce the mechanical properties of the material [45]. The complete dehydration of C-S-H at this stage also leads to a loss of its gel-like characteristics, transforming into a brittle, low-cohesion phase [47].

$Ca(OH)_2$ decomposition: $Ca(OH)_2$ is another important phase in 3DPC and remains stable at about 400 °C, as seen in Fig. 14(b). It crystallizes in a hexagonal structure, contributing to the mechanical strength of the cement matrix. However, even at lower temperatures, $Ca(OH)_2$ can contribute to crack formation if excess water vapor is released from its decomposition. When the temperature exceeds 400 °C, $Ca(OH)_2$ begins to decompose into calcium oxide (CaO) and water vapor. This phase transition results in a volume loss and the formation of microvoids, which further propagate cracks throughout the concrete matrix. The water vapor released accelerates the dehydration of C-S-H and induces internal stresses, further contributing to structural degradation. The decomposition of $Ca(OH)_2$ and the formation of CaO leave behind a weaker material. CaO is less capable of providing structural support, and its reaction with ambient moisture to form calcium hydroxide is not immediate, contributing to the deterioration of the material's mechanical properties.

$CaCO_3$ and decarbonation: Before 600 °C, $CaCO_3$ remains relatively stable, providing mechanical reinforcement to the concrete [48]. $CaCO_3$, especially in the form of calcite, offers a rigid crystalline structure that adds to the overall strength of the material, as seen in Fig. 14(b). Once the temperature exceeds 600 °C, $CaCO_3$ begins to undergo decarbonation, transforming into CaO and releasing CO_2 gas. This reaction leads to a loss of mass and the formation of internal voids as the CO_2 escapes, significantly weakening the material. The newly formed CaO, combined with the voids left by the escaping CO_2, exacerbates the porosity of the concrete and accelerates crack formation.

In summary, the mechanical properties and microstructural evolution of 3D printed concrete under high temperature conditions are the result of a combination of factors. Water evaporation, decomposition of chemical components (e.g., $Ca(OH)_2$ and $CaCO_3$), as well as thermal expansion and crack extension interact with each other in different temperature intervals. They together contribute to the structural deterioration of 3DPC. Through a deeper understanding of these mechanisms, the refractory properties of 3D printed concrete can be improved in the future by optimizing the concrete formulation and 3D printing process, it will provide more reliable technical support for its use in real building applications.

4. Conclusions

This study systematically investigates the effects of high temperatures on the interlayer strength, microstructural morphology, hydration products, and pore structure of 3D printed concrete (3DPC). The degradation mechanisms of 3DPC interlayers under elevated temperature conditions were explored through interlayer strength tests and comprehensive analyses using XRD, SEM, TG, and X-CT techniques. The findings can be summarized as follows.

(1) The mass loss rate of 3DPC increases as temperature rises, attributed to the evaporation of both free and bound water, decomposition of calcium hydroxide ($Ca(OH)_2$), and thermal decomposition of calcium carbonate ($CaCO_3$). The bond strength

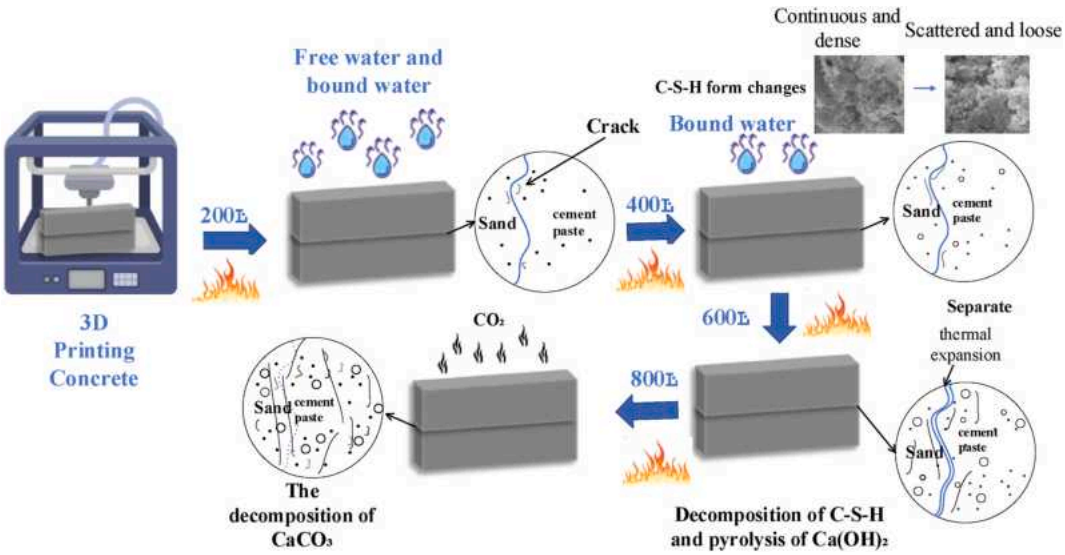

Fig. 13. Mechanism diagram of 3DPC interlayer strength decline at elevated temperature.

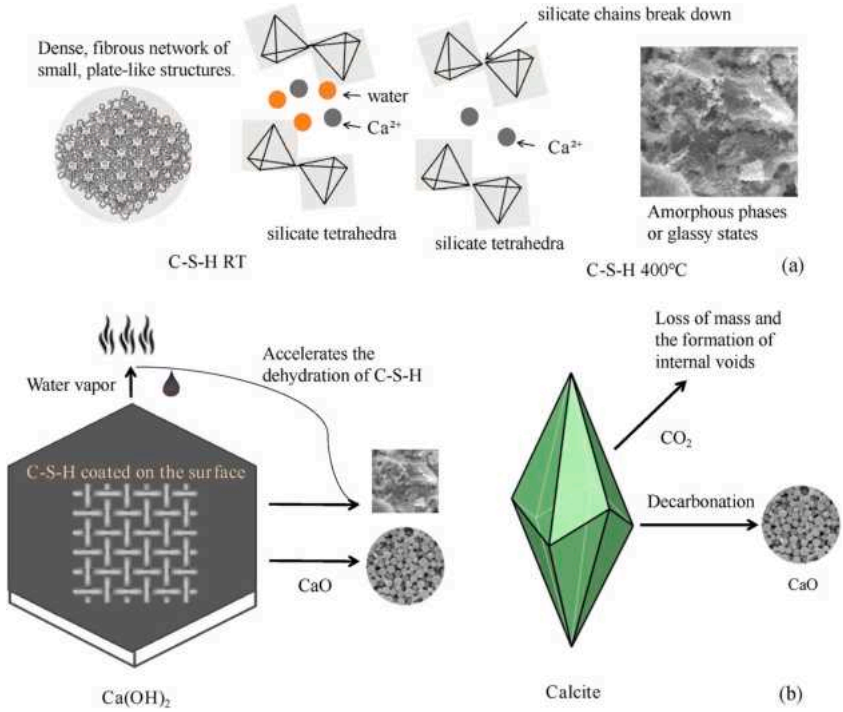

Fig. 14. Schematic diagram illustrating the degradation mechanism of 3D printed concrete (3DPC) interlayer strength at elevated temperatures: (a) C-S-H strength mechanism (b) Crystal strength failure mechanism.

between 3DPC interlayers decreases sharply with increasing temperature and duration of exposure. At 800 °C, this bond strength is reduced by over 90 %, indicating a substantial loss in the structural integrity of 3DPC.

(2) The high temperatures increases the number and size of pores in the concrete matrix. Pore distribution and volume alter notably, with a rise in the presence of small pores at higher temperatures due to water release and the decomposition of hydrated phases. This heightened porosity, particularly in the interlayer, exacerbates structural weakening, as it creates pathways for crack initiation and propagation.

(3) Cracks are more prevalent and develop more extensively in regions with higher porosity, particularly at the sand-cement interface. When temperatures exceed 400 °C, differential thermal expansion and the progressive breakdown of $Ca(OH)_2$

cause substantial crack growth, with a marked escalation in microcracking. Above 600 °C, the complete decomposition of Ca $(OH)_2$ and $CaCO_3$ results in large, interconnected cracks, leaving the material highly porous and structurally compromised.

While this study provides valuable insights into the high-temperature performance of 3DPC, there are limitations to consider. Experiments were conducted under controlled laboratory conditions, lacking factors present in real fire scenarios, such as thermal shock and structural loads. This study has certain limitations, including a small sample size, a limited temperature range, and a focus on a single material composite. In future work, we plan to address these limitations by testing other proportions and incorporating fibres to improve the fire resistance of 3DPC. These experiments will provide deeper insights into optimizing 3DPC for high temperature applications.

CRediT authorship contribution statement

Biao Zhou: Supervision, Funding acquisition. **Hongru Zhou:** Writing – review & editing, Writing – original draft, Data curation. **Hideki Yoshioka:** Supervision, Methodology, Investigation. **Takafumi Noguchi:** Visualization, Supervision, Methodology. **Kai Wang:** Validation, Methodology, Formal analysis. **Bochao Sun:** Writing – review & editing, Investigation, Conceptualization. **Gaochuang Cai:** Methodology, Formal analysis, Conceptualization. **Yike Guo:** Visualization, Methodology, Conceptualization. **Dianchao Wang:** Writing – review & editing, Project administration, Investigation. **Weijian Zhao:** experiemtnal test.

Declaration of competing interest

The authors declared that they have no conflicts of interest to this work.We declare that we do not have any commercial or associative interest that represents a conflict of interest in connection with the work submitted.

Acknowledgment

This work was supported by the National Natural Science Foundation of China (No.52374248), Beijing Nova Program (No. Z211100002121102), the Tianjin Science and Technology Plan Project (No.22JCZDJC00880, No.22JCZDJC00900), the Ministry of Education Chunhui Plan Collaborative Research Project (No.HZKY202200132), the Key-Area Research and Development Program of Guangdong Province (No. 2024B1111080002), the Ordos key research and development program (No. YF20240026) and the Key Laboratory of Fire Protection Technology for Industry and Public Building Ministry of Emergency Management (No.2023KLIB02).

Data availability

Data will be made available on request.

References

[1] M. Xia, J. Sanjayan, Method of formulating geopolymer for 3D printing for construction applications, Mater. Des. 110 (2016) 382–390.
[2] F. Bos, R. Wolfs, Z. Ahmed, T. Salet, Additive manufacturing of concrete in construction: potentials and challenges of 3D concrete printing, Virtual Phys. Prototyp. 11 (3) (2016) 209–225, https://doi.org/10.1080/17452759.2016.1209867.
[3] G. De Schutter, K. Lesage, V. Mechtcherine, V.N. Nerella, G. Habert, I. Agusti-Juan, Vision of 3D printing with concrete — technical, economic and environmental potentials, Cement Concr. Res. 112 (2018) 25–361.
[4] E. Harrison, A. Berenjian, M. Seifan, Recycling of waste glass as aggregate in cement-based materials, Environmental Science and Ecotechnology 4 (2020) 100064.
[5] P. Barve, A. Bahrami, S. Shah, Geopolymer 3D printing: a comprehensive review on rheological and structural performance assessment, printing process parameters, and microstructure, Frontiers in Materials 10 (2023), https://doi.org/10.3389/fmats.2023.1241869.
[6] J. Sanjayan, Current progress of 3D concrete printing technologies. Proceedings of the 34th International Symposium on Automation and Robotics in Construction (ISARC), Tribun EU, s.r.o., Brno, 2017, pp. 260–267.
[7] H.G. Şahin, Y. Kaya, F.E. Akgümüş, N. Mardani, A. Mardani, J. Assaad, B. Hamad, Degradation of mechanical properties of 3D fiber reinforced printed concrete mixtures exposed to elevated temperatures, Case Stud. Constr. Mater. 22 (2025) e04506.
[8] T. Pan, Y. Jiang, X. Ji, Interlayer bonding investigation of 3D printing cementitious materials with fluidity-retaining polycarboxylate superplasticizer and high-dispersion polycarboxylate superplasticizer, Constr. Build. Mater. 330 (2022) 127151.
[9] D. Nemova, E. Kotov, D. Andreeva, S. Khorobrov, V. Olshevskiy, I. Vasileva, D. Zaborova, T. Musorina, Experimental study on the thermal performance of 3D-printed enclosing structures, Energies 15 (12) (2022) 4230.
[10] T. Suntharalingam, P. Gatheeshgar, I. Upasiri, K. Poologanathan, B. Nagaratnam, M. Corradi, D. Nuwanthika, Fire performance of innovative 3D printed concrete composite wall panels – a Numerical Study, Case Stud. Constr. Mater. 15 (2021) e00586.
[11] S. Krishna Priya Rao, T. Tadepalli, High-temperature behaviour of concrete: a review, in: R.K. Pancharathi, C.K.Y. Leung, J.M. Chandra Kishen (Eds.), Low Carbon Materials and Technologies for a Sustainable and Resilient Infrastructure, Springer Nature Singapore, Singapore, 2024, pp. 167–186.
[12] G. Biradar, N. Ramanna, Performance of concrete at elevated temperatures: a review, in: K.S. Sreekeshava, S. Kolathayar, N. Vinod Chandra Menon (Eds.), Recent Advances in Structural Engineering, Springer Nature Singapore, Singapore, 2024, pp. 225–238.
[13] M. Amran, S.-S. Huang, A.M. Onaizi, G. Murali, H.S. Abdelgader, Fire spalling behavior of high-strength concrete: a critical review, Constr. Build. Mater. 341 (2022) 127902.
[14] S. Ramzi, H. Hajiloo, The effects of supplementary cementitious materials (SCMs) on the residual mechanical properties of concrete after exposure to high temperatures—review, Buildings (2023).
[15] I. Hager, A. Golonka, R. Putanowicz, 3D printing of buildings and building components as the future of sustainable construction? Procedia Eng. 151 (2016) 292–299.
[16] M. Nodehi, F. Aguayo, S.E. Nodehi, A. Gholampour, T. Ozbakkaloglu, O. Gencel, Durability properties of 3D printed concrete (3DPC), Autom. ConStruct. 142 (2022) 104479.

[17] A.H. Akca, N. Özyurt, Effects of re-curing on residual mechanical properties of concrete after high temperature exposure, Constr. Build. Mater. 159 (2018) 540–552.
[18] K. Zhang, W. Lin, Q. Zhang, D. Wang, S. Luo, Evaluation of anisotropy and statistical parameters of compressive strength for 3D printed concrete, Constr. Build. Mater. 440 (2024) 137417.
[19] K.-H. Ler, C.-K. Ma, C.-L. Chin, I.S. Ibrahim, K.H. Padil, M.A.I. Ab Ghafar, A.A. Lenya, Porosity and durability tests on 3D printing concrete: a review, Constr. Build. Mater. 446 (2024) 137973.
[20] J. Yuan, W. Chen, X. Tan, W. Yang, D. Yang, H. Yu, B. Zhou, B. Yang, Study on the permeability characteristics of foamed concrete using a pore-scale model from X-ray microcomputed tomography image reconstruction and numerical simulation, J. Mater. Civ. Eng. 33 (6) (2021) 04021117, https://doi.org/10.1061/(ASCE)MT.1943-5533.0003735.
[21] X. Gao, S. Qi, X. Kuang, Y. Su, J. Li, D. Wang, Fused filament fabrication of polymer materials: a review of interlayer bond, Addit. Manuf. 37 (2021) 101658.
[22] Z. Pan, D. Si, J. Tao, J. Xiao, Compressive behavior of 3D printed concrete with different printing paths and concrete ages, Case Stud. Constr. Mater. 18 (2023) e019499.
[23] A.U. Rehman, J.-H. Kim, 3D concrete printing: a systematic review of rheology, mix designs, mechanical, microstructural, and durability characteristics, Materials (2021).
[24] S.D. Anitha Selvasofia, E. Sarojini, G. Moulica, S. Thomas, M. Tharani, P.T. Saravanakumar, P. Manoj Kumar, Study on the mechanical properties of the nanoconcrete using nano-TiO2 and nanoclay, Mater. Today Proc. 50 (2022) 1319–1325.
[25] B. Sun, R. Dominicus, E. Dong, P. Li, Z. Ye, W. Wang, Predicting the strength development of 3D printed concrete considering the synergistic effect of curing temperature and humidity: from perspective of modified maturity model, Constr. Build. Mater. 427 (2024) 136291.
[26] J. Xiao, N. Han, L. Zhang, S. Zou, Mechanical and microstructural evolution of 3D printed concrete with polyethylene fiber and recycled sand at elevated temperatures, Constr. Build. Mater. 293 (2021) 123524.
[27] L. Wang, W. Lin, H. Ma, D. Li, Q. Wang, Mechanical and microstructural properties of 3D-printed aluminate cement based composite exposed to elevated temperatures, Constr. Build. Mater. 353 (2022) 129144.
[28] I. Janotka, S.C. Mojumdar, Thermal analysis at the evaluation of concrete damage by high temperatures, J. Therm. Anal. Calorim. 81 (1) (2005) 197–203, https://doi.org/10.1007/s10973-005-0767-6.
[29] S. Hou, Z. Duan, J. Xiao, J. Ye, A review of 3D printed concrete: performance requirements, testing measurements and mix design, Constr. Build. Mater. 273 (2021) 121745.
[30] B. Sun, Q. Zeng, D. Wang, W. Zhao, Sustainable 3D printed mortar with CO2 pretreated recycled fine aggregates, Cement Concr. Compos. 134 (2022) 104800.
[31] L. Li, Q. Wang, G. Zhang, L. Shi, J. Dong, P. Jia, A method of detecting the cracks of concrete undergo high-temperature, Constr. Build. Mater. 162 (2018) 345–358.
[32] H.E. Yücel, S. Özcan, Strength characteristics and microstructural properties of cement mortars incorporating synthetic wollastonite produced with a new technique, Constr. Build. Mater. 223 (2019) 165–176.
[33] Y. Che, H. Yang, Hydration products, pore structure, and compressive strength of extrusion-based 3D printed cement pastes containing nano calcium carbonate, Case Stud. Constr. Mater. 17 (2022) e01590.
[34] H.E.D.H. Seleem, A.M. Rashad, T. Elsokary, Effect of elevated temperature on physico-mechanical properties of blended cement concrete, Constr. Build. Mater. 25 (2) (2011) 1009–1017.
[35] G.-F. Peng, Z.-S. Huang, Change in microstructure of hardened cement paste subjected to elevated temperatures, Constr. Build. Mater. 22 (4) (2008) 593–599.
[36] X.M. Aretxabaleta, J. López-Zorrilla, I. Etxebarria, H. Manzano, Multi-step nucleation pathway of CSH during cement hydration from atomistic simulations, Nat. Commun. 14 (1) (2023) 7979.
[37] Z. Lyu, A. Shen, S. Mo, Z. Chen, Z. He, D. Li, X. Qin, Life-cycle crack resistance and micro characteristics of internally cured concrete with superabsorbent polymers, Constr. Build. Mater. 259 (2020) 119794.
[38] E. John, B. Lothenbach, Cement hydration mechanisms through time – a review, J. Mater. Sci. 58 (24) (2023) 9805–9833, https://doi.org/10.1007/s10853-023-08651-9.
[39] Q. Zhang, G. Ye, Dehydration kinetics of Portland cement paste at high temperature, J. Therm. Anal. Calorim. 110 (1) (2012) 153–158, https://doi.org/10.1007/s10973-012-2303-9.
[40] S.K. Handoo, S. Agarwal, S.K. Agarwal, Physicochemical, mineralogical, and morphological characteristics of concrete exposed to elevated temperatures, Cement Concr. Res. 32 (7) (2002) 1009–1018.
[41] C. Ge, X. Chen, Y. Gong, X. Kong, F. Chen, Effect of high temperature on micro-structure and mechanical properties of fiber-reinforced cement-based composites, Crystals (2024).
[42] M.C. Alonso, U. Schneider, Degradation reactions in concretes exposed to high temperatures, in: P. Pimienta, R. Jansson McNamee, J.-C. Mindeguia (Eds.), Physical Properties and Behaviour of High-Performance Concrete at High Temperature: State-Of-The-Art Report of the RILEM Technical Committee 227-HPB, Springer International Publishing, Cham, 2019, pp. 5–40.
[43] P.A. Bonnaud, Q. Ji, K.J. Van Vliet, Effects of elevated temperature on the structure and properties of calcium–silicate–hydrate gels: the role of confined water, Soft Matter 9 (28) (2013) 6418–6429, https://doi.org/10.1039/C3SM50975C.
[44] Y. He, X. Zheng, L. Lü, S. Yu, G. Deng, S. Hu, Dehydration characteristics of C-S-H with Ca/Si ratio 1.0 prepared via precipitation, J. Wuhan Univ. Technol.-Materials Sci. Ed. 33 (3) (2018) 619–624, https://doi.org/10.1007/s11595-018-1869-x.
[45] B.H. Cho, W. Chung, B.H. Nam, Molecular dynamics simulation of calcium-silicate-hydrate for nano-engineered cement composites—a review, Nanomaterials (2020).
[46] E. Duque-Redondo, P.A. Bonnaud, H. Manzano, A comprehensive review of C-S-H empirical and computational models, their applications, and practical aspects, Cement Concr. Res. 156 (2022) 106784.
[47] A. Madadi, J. Wei, Characterization of calcium silicate hydrate gels with different calcium to silica ratios and polymer modifications, Gels (2022).
[48] M. Cao, L. Li, H. Yin, X. Ming, Microstructure and strength of calcium carbonate (CaCO3) whisker reinforced cement paste after exposed to high temperatures, Fire Technol. 55 (6) (2019) 1983–2003, https://doi.org/10.1007/s10694-019-00839-3.